

# Assessing the Acidity of High Silica Chabazite H–SSZ-13 by FTIR Using CO as Molecular Probe: Comparison with H–SAPO-34

Silvia Bordiga,<sup>†</sup> Laura Regli,<sup>†</sup> Donato Cocina,<sup>†</sup> Carlo Lamberti,<sup>†</sup> Morten Bjørgen,<sup>‡</sup> and Karl Petter Lillerud<sup>\*‡</sup>

Dipartimento di Chimica IFM and NIS Centre of Excellence, Via P. Giuria 7, I-10125 Torino, Italy, and Department of Chemistry, University of Oslo, P.O. Box 1033, N-0315 Oslo, Norway

Received: October 4, 2004; In Final Form: November 25, 2004

Zeolitic materials based on the chabazite topology, such as H–SAPO-34, possess unique shape-selectivity properties for converting methanol into light olefins. In addition to the topology, zeolite acidity is inherently linked to catalyst activity and selectivity. The acidic properties of high silica chabazite (H–SSZ-13) have attracted much attention in the past decade because the material represents an idealized model system having one acidic site per cage. Conclusions drawn so far have essentially been founded on quantum chemical methods. An experimentally based benchmark of the acidity of H–SSZ-13 has hitherto not been available. In this work, transmission FTIR spectroscopy provides a description of the different acidic sites of H–SSZ-13 by using CO as molecular probe at 70 K. The results demonstrate that H–SSZ-13 is a strongly Brønsted acidic material, essentially having two distinct *families* of acidic sites. In contrast to numerous preceding reports, we find it fundamental to consider proton distributions among all four possible sites, and do not delimit the interpretations to only two sites. The present data consistently suggest the most abundant family of protons to have three members being located on different crystalline positions on the eight-membered-ring window giving access to the chabazite cage. Consequently, these protons are exposed to two neighboring cages. The second, and less abundant family, is constituted by only one site that is situated on the six-membered ring defining the top/bottom of the barrel-shaped chabazite cage. This proton is therefore only exposed to one cage and requires a higher CO pressure to form adducts. Toward CO, both families of sites possess the same acidity. Parallel experiments were also carried out for the isostructural and commercially important H–SAPO-34 having an equal density of acidic sites. This is the first attempt to directly compare, on an experimental basis, the acidity of these two materials.

## 1. Introduction

Conversion of hydrocarbons and methanol into more valuable products has relied heavily on heterogeneous acidic catalysts, such as zeolites, throughout several decades. The continuous interest in developing more selective and deactivation resistant catalysts has motivated the catalysis community to reach a fundamental mechanistic understanding of these reaction systems. To advance such knowledge, an adequate description of the active acid sites is highly desirable. For zeolites the acidity, along with the size of the micropores, is inherently linked to activity, selectivity, and catalyst lifetime.

Zeolite structures based on the chabazite topology show unique shape-selectivity properties for converting methanol into light olefins (MTO).<sup>1–3</sup> Indeed, H–SAPO-34, the silicoaluminophosphate analogue of chabazite, is the catalyst of the UOP/Norsk Hydro MTO technology which currently is under commercialization. Chabazite has traditionally been synthesized with a relatively high aluminum content (Si/Al = 2–3). This work is, however, devoted to the acidic properties of zeolite H–SSZ-13, which is a low aluminum chabazite variant. A parallel set of data has also been obtained for H–SAPO-34 in order to examine the effect on acidity generated by Al defects

in a silica lattice compared to that generated by Si defects in an alumina–phosphate lattice.

In addition to quantum chemical modeling, neutron powder diffraction, and a variety of spectroscopic techniques, such as Fourier transform infrared (FTIR) and NMR, have been used, also with the aid of molecular probes, to describe the local structure of the acid sites in H–chabazite and H–SAPO-34.<sup>4–12</sup> Among these two materials, the zeolite variant has been suggested to possess the stronger Brønsted acidic properties.<sup>7,10</sup> Both the O–H bond lengths and the vibrational frequencies are consistent with the proton being more weakly bound to the framework in the zeolite than in the SAPO analogue.<sup>7</sup> A further evaluation of this claim by comparing two isostructural SAPO and aluminosilicate based materials is essential for understanding their catalytic abilities. To reduce the number of permutations to be considered, a major part of the theoretical work has dealt with H–SSZ-13 rather than high aluminum chabazite.<sup>9,12–14</sup> In this work, we have aimed at providing a link between the existing theoretical data on H–SSZ-13 and the corresponding data obtained with FTIR. Whereas the acidic properties of high aluminum H–chabazite and H–SAPO-34 are well documented in the literature, there is currently no such experimentally based data on H–SSZ-13.

The left part of Figure 1 is a schematic T-atom illustration of a chabazite cage. The black bold part of the framework is shown with the different protons highlighted in the right part of Figure 1. Thus, the right part of the figure shows one eight-

\* To whom correspondence should be addressed. Phone: + 47 22 85 54 57. Fax: + 47 22 85 54 41. E-mail address: kpl@kjemi.uio.no.

<sup>†</sup> Dipartimento di Chimica IFM and NIS Centre of Excellence.

<sup>‡</sup> University of Oslo.

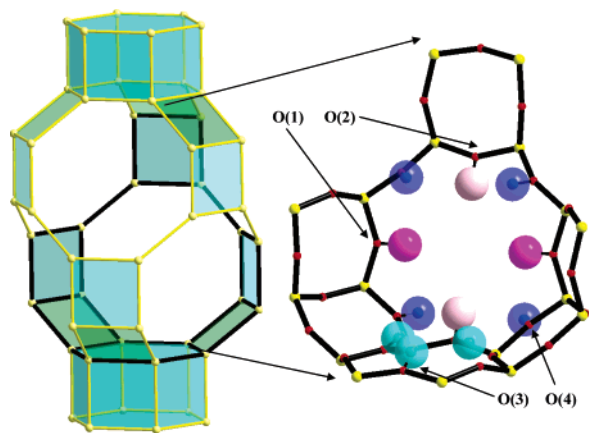


**Figure 1.** Left: T-atom drawing of a chabazite cage. The black bold part of the framework is extracted and presented to the right. Right: one eight-membered-ring window and one of the six-membered rings with the four proton positions drawn. Symmetry-equivalent positions cause the positions to be represented with two, three, or four protons. The sizes of the proton spheres represent half the van der Waals radius. Protons attached to O(3) (cyan) are not exposed to the eight-membered-ring window and are thus distinctive from those attached to O(1) (purple), O(2) (pink), and O(4) (blue).

membered-ring window and one of the six-membered rings with the four proton positions drawn. The chabazite topology might be described as layers of double six-membered rings that are interconnected by units of four-membered rings. The double six-membered-ring layers stack in an ABC sequence. This leads to a framework with a regular array of barrel-shaped cages interconnected by eight-membered-ring windows. The chabazite structure contains only one unique tetrahedral site but four different oxygen atoms in the asymmetric unit, giving four possible acid site configurations, depending on to which of the oxygen atoms the proton is attached. According to the nomenclature introduced previously,<sup>8</sup> the four oxygens belong to the following ring systems (see Figure 1): O(1) is the oxygen forming the bridge between the two six-membered rings giving the double six-membered-ring units. O(1) belongs to two four-membered rings and one eight-membered ring; O(2) and O(3) have alternating positions in the six-membered rings, where O(2) is a part of the eight-membered-ring windows and not the four-membered rings bridging the double six-membered rings. Hence, O(2) is a member of one four-membered ring, one six-membered ring, and one eight-membered ring. O(3) is a member of two four-membered rings and one six-membered ring, and O(4) forms the bridge between the double six-membered rings. O(4) belong to one four-membered ring and two eight-membered rings. Figure 1 demonstrates that all site topologies are rather similar and that all protons should be exposed to the cage. A minor relevant difference is that O(1), O(2), and O(4) are all parts of the eight-membered-ring window, delimiting the CHA cage, while O(3) is protruding inside the cage and is not part of the open window of the cage. This characteristic, together with the fact that a proton linked to O(3) could interact with an oxygen of a six-membered-ring window, forming an H-bond, makes this site slightly different from the others.

## 2. Experimental Section

The H-SAPO-34 sample was synthesized and calcined in accordance with standard procedures.<sup>15</sup> Zeolite SSZ-13 was obtained by following a hydrothermal preparation procedure described elsewhere.<sup>16</sup> The acidic form of SSZ-13 was obtained by a controlled calcination procedure, aiming at preserving the

**TABLE 1: Surface Areas of H-SSZ-13 and H-SAPO-34 Obtained by N<sub>2</sub> Adsorption at 77 K**

material	$S_{\text{BET}}$ , m <sup>2</sup> /g	$S_{\text{Langmuir}}$ , m <sup>2</sup> /g	$V_{\text{micropore}}$ , <sup>a</sup> mL/g
H-SAPO-34	547	724	0.231
H-SSZ-13	638	843	0.277

<sup>a</sup> From  $t$ -plot.

crystallinity of the material. The template removal was carried out in a pure oxygen flow (20 mL/min) in a fixed bed tubular quartz reactor according to the following procedure: The as-synthesized sample was initially heated to 573 K and left at this temperature for 12 h. The temperature was slowly increased to 773 K and kept isothermal for another 12 h. Powder X-ray diffraction (XRD; measured on a Siemens D5000 diffractometer using Cu K $\alpha_1$  radiation) confirmed a pure SSZ-13 phase. Qualitative elemental analysis and sample morphology were examined using a Philips XL 30 scanning electron microscope. The Si/Al ratio was 11.6, and the average particle size was in the range 5–10  $\mu\text{m}$ . Thermogravimetric analysis (TGA–DTC) of the as-synthesized sample was performed with a Rheometric Scientific STA 1500 instrument at a heating rate of 10 K/min in a pure oxygen flow. Temperature-resolved powder XRD data were recorded on a Siemens D500 instrument equipped with a Brown high temperature sample holder, modified for automatic temperature control and controlled atmosphere. The sample was smeared on a platinum filament, and data were collected in steps of 50 K in the temperature range 373–1373 K in a pure oxygen flow. SAPO-34 is known to be a more thermally resistant material than SSZ-13, and the calcination was thus carried out at 873 K for 4 h according to standard procedures.<sup>15</sup>

The surface areas of H-SSZ-13 and H-SAPO-34 were obtained by N<sub>2</sub> adsorption at 77 K. The volumetric measurements were performed on a Micromeritics ASAP 2010 sorption analyzer. Prior to the adsorption measurements, the samples were subjected to a thermal treatment, identical to that of the respective IR experiments. BET area,<sup>17</sup> Langmuir area,<sup>18</sup> and micropore volume (from the  $t$ -plot)<sup>19a–e</sup> (using the Harkins and Jura equation)<sup>19f</sup> obtained from the N<sub>2</sub> adsorption measurements are reported in Table 1.

FTIR transmission spectra were collected using compressed self-supported zeolite wafers. Prior to the experiments, the samples were pretreated in situ at temperatures up to 773 K under high vacuum to remove water and other adsorbed impurities. CO was dosed from a vacuum line permanently attached to the IR cell kept at 70 K. This represents a remarkable improvement with respect to conventional low temperature IR experiments, nominally performed at 77 K (but actually at 100–120 K due to the heating effect of the IR beam). To perform transmission FTIR measurements on catalysts below liquid nitrogen temperature an ad hoc conceived prototype has been designed by coupling a properly modified closed circuit liquid helium Oxford CCC 1204 cryostat with a Bruker Equinox-55 FTIR spectrometer (equipped with a MCT detector). A detailed description of this instrument is reported elsewhere.<sup>20</sup> The spectra were collected at 2 cm<sup>−1</sup> resolution.

## 3. Results and Discussion

**3.1. Thermal Behavior of SSZ-13 upon Template Removal.** Rather few experimental reports on the SSZ-13 material are currently available. Hence, elucidating the thermal stability and finding appropriate conditions for a complete removal of the template without introducing additional structural defects has therefore been paid some attention in this work.

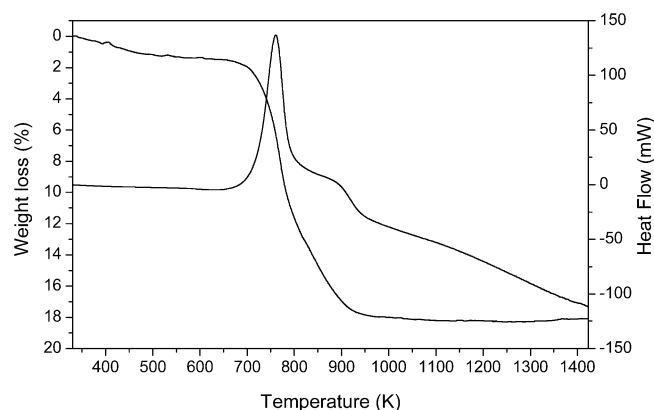


**Figure 2.** TGA–DTC profiles for oxidative removal of template from as-synthesized SSZ-13 collected at a heating rate of 10 K/min.

**3.1.1. Thermogravimetric Analysis.** The weight loss and heat flow profiles up to 1423 K for as-synthesized SSZ-13 are shown in Figure 2. The rather bulky template ions (trimethyladaman-tanammonium) prevent the zeolite from adsorbing other molecules in any large quantity, and only a small weight loss of 1.4%, due to desorption of water, is observed upon heating the as-synthesized sample.<sup>21</sup> This weight loss corresponds to 1.2 water molecules per unit cell. The oxidative removal of the template, starting at 643 K, is an exothermic process as indicated by the DSC signal with a peak maximum at 760 K. The template removal appears to take place in two steps. The first step most likely represents a decomposition of the template as such. Upon heating, the template may convert into more thermally stable aromatic compounds that are oxidized in the second step. At about 980 K, all hydrocarbons are in this case removed from the sample. The total weight reduction due to removal of the template was about 17%, a value virtually the same as the one calculated (18.6%) by considering one template ion per cage.

To elucidate structural changes related to calcination, an experiment with stepwise heating was carried out in parallel to powder XRD measurements performed in steps of 50 K (110 min at each preselected temperature) in the temperature range 643–1073 K. The experiment showed that, after treatment of the sample at 773 K, a significant exothermic DTC signal could still be observed when the sample was heated to 823 K. This means that 110 min at 773 K is insufficient to remove all the organic material from SSZ-13. Reassuringly, the weight loss due to removal of the template was also in this experiment found to be 17%.

**3.1.2. Temperature-Resolved XRD.** Figure 3 shows a three-dimensional representation of the progressive change in the powder diffraction patterns of as-synthesized SSZ-13 in the temperature range 373–1373 K in a pure oxygen flow. The parallel stepwise thermogravimetric experiment described in section 3.1.1 showed that a temperature of 823 K is necessary, under the given set of conditions, to remove all the organic material from the sample. This agrees well with the XRD experiments presented in Figure 3, since the diffraction pattern intensities change significantly up to 823 K and then level off. The intensities decline at temperatures higher than 1223 K as the open characteristic structure transforms into a dense silicate. A rather comprehensive work related to in situ powder XRD of template removal from zeolites is provided by ref 22.

**3.2. CO as Base for Probing the Acidity of H-SSZ-13 and H-SAPO-34 by FTIR at 70 K.** Vibrational spectroscopy of adsorbed CO can conveniently be employed to probe the electrostatic fields generated by hydroxyl groups in, e.g., zeolites.<sup>23–25</sup> Interactions between the dipolar CO molecule (via the carbon end) and centers having a net positive charge shift the C–O stretching frequency of the free molecule (2138 cm<sup>−1</sup> liquidlike)<sup>26</sup> to higher values, and the magnitude of this hypsochromic shift is related to the corresponding field strength in the zeolite.<sup>27</sup> In a parallel way, upon interaction with CO, bands associated with Brønsted acidic sites in a zeolite move to lower frequencies, with a shift proportional to their acidic strength. Measuring the perturbations of the vibrational modes of Brønsted sites induced by a base is the classical way to study their acidity.

**3.2.1. Interaction between CO and H-SSZ-13.** Figure 4 presents FTIR spectra of increasing doses of CO adsorbed at 70 K on a fully dehydrated H-SSZ-13 zeolite. Part a covers the OH stretching ( $\nu(\text{OH})$ ) region, and part b reports the C–O stretching frequencies. The spectrum of the activated sample prior to CO adsorption is represented by spectrum 1 (bold curve) in the lower part of Figure 4a. The vibrational properties of H-SSZ-13 are characterized by a multiplicity of  $\nu(\text{OH})$  bands related to weakly acidic silanol groups and strongly acidic Brønsted sites. More specifically, the activated sample (spectrum 1) shows a complex absorption with a maximum at 3740 cm<sup>−1</sup> representing  $\nu(\text{OH})$  modes of virtually isolated silanol groups located on the internal or external surface of the zeolite.<sup>28,29</sup> The component on the low-frequency tail of this band (maximum at 3712 cm<sup>−1</sup>) is related to vicinal silanol groups, that is, silanol groups where only the oxygen participates in H-bonding and the proton can be considered to be more or less free.<sup>30</sup> At lower frequencies, in a region where absorptions are commonly

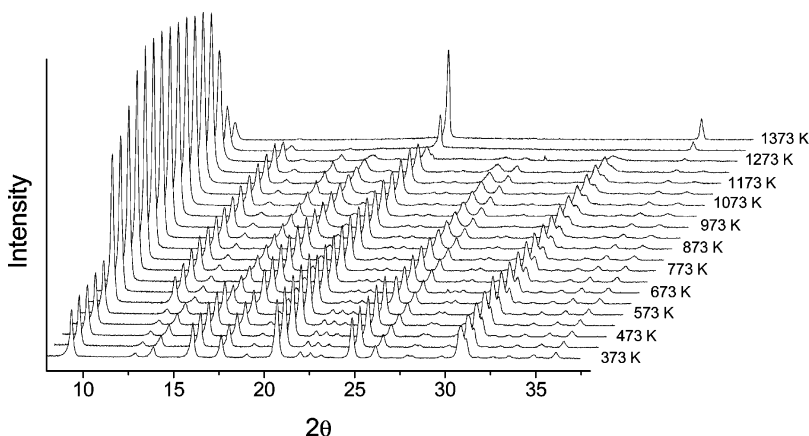


**Figure 3.** Three-dimensional representation of high-temperature (373–1373 K) powder X-ray data for as-synthesized SSZ-13 collected in a pure oxygen flow.



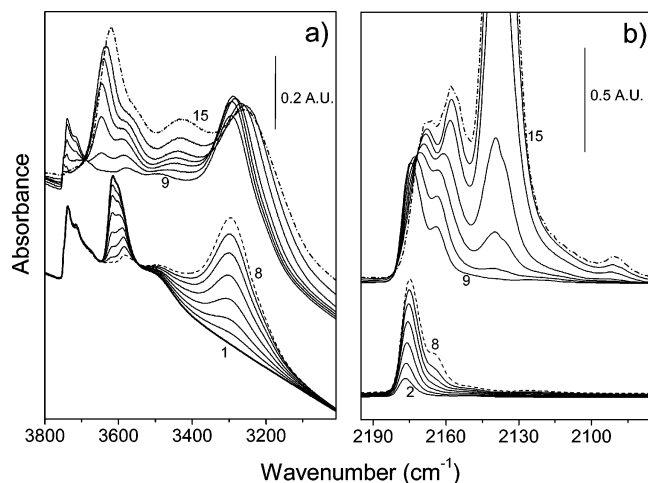


**Figure 4.** IR spectra of increasing dosages of CO at 70 K on H-SSZ-13 outgassed at 773 K. (a) OH stretching region (spectrum 1 represents the pretreated zeolite); (b) CO region (background-subtracted spectra). The spectra have been divided into two subsets to distinguish CO interactions with strong Brønsted sites (spectra 2–8) from those with silanols (spectra 9–15). Spectrum 8 represents the highest CO coverage where silanols are still nearly unperturbed.

observed for protonic zeolites, bridging Brønsted acidic OH groups give rise to a composite band with a maximum at 3616  $\text{cm}^{-1}$  and a shoulder at 3600  $\text{cm}^{-1}$ . The asymmetric shape of this band has previously been claimed to arise from two distinct Brønsted sites,<sup>8</sup> an interpretation that might be an oversimplification of the system (vide infra). Finally, a broad component at about 3500  $\text{cm}^{-1}$  suggests the presence of silanol groups interacting through medium-strong H-bonds in so-called silanol nests (i.e., structural defects).<sup>30,31</sup> This component can be eliminated upon treatment at higher temperatures where silanol groups situated in nests condense to Si–O–Si bridges under concomitant water elimination.<sup>30</sup> Unfortunately, elimination of water at high temperatures may lead to hydrolysis of structural O–Al–O bridges with progressive formation of extralattice or partially extralattice aluminum.<sup>28</sup> It is worth noticing that such a hydrolysis can easily be revealed by absorptions around 3660–3680 or 3780  $\text{cm}^{-1}$ , and accordingly, the template removal procedure adopted in this work did not create any extralattice or partially extralattice aluminum.

The spectra of increasing CO coverages at 70 K are reported in two series in Figure 4, to distinguish a first stage where strong Brønsted sites interact (spectra 2–8) from a second stage where interactions with silanols and/or polyadditions take place (spectra 9–15). Clearly, increasing CO coverage leads to a gradual consumption of the  $\nu(\text{OH})$  modes of Brønsted sites related to the so-called high-frequency (HF) band at 3616  $\text{cm}^{-1}$ .<sup>8</sup> In addition, the erosion of this band allows pinpointing the position of the low-frequency (LF) component, now at 3584  $\text{cm}^{-1}$ , that was observed as a shoulder on the HF band in the spectrum of the unperturbed sample (spectrum 1).<sup>8</sup> Note that the LF band is less intense than the HF band, and as its extinction coefficient is higher, this observation suggests that the LF sites correspond to a minor fraction of the total set of sites in H-SSZ-13 (vide infra). The LF component starts to be consumed only at higher CO coverages. Parallel to the erosion of the Brønsted bands, red-shifted  $\nu(\text{OH})$  modes of  $\text{OH}\cdots\text{CO}$  adducts appear at 3300  $\text{cm}^{-1}$  ( $\Delta\nu(\text{OH}) = -316 \text{ cm}^{-1}$ ). The presence of a single red-shifted component suggests that the acidity of the two families of Brønsted sites, measured by CO, is equivalent. This means that if the HF and LF families are essentially different under vacuum conditions (owing to a different neighbor environment;

see the Introduction) the resulting  $\text{OH}\cdots\text{CO}$  complexes cannot be differentiated by IR spectroscopy. Spectrum 8 represents the CO pressure where virtually all strong Brønsted sites are interacting with CO, whereas silanol groups are still mainly unperturbed.

The formation of hydrogen-bonded  $\text{OH}\cdots\text{CO}$  adducts is also accompanied by a perturbation of the internal vibrations of the base. The perturbation of the  $\nu(\text{CO})$  mode is represented by the background-subtracted spectra 2–15 in Figure 4b. Starting from the lowest CO coverage (spectrum 2), a component is clearly visible at 2177  $\text{cm}^{-1}$ . The evident blue shift with respect to the free molecule ( $\nu(\text{CO})$  liquidlike 2138  $\text{cm}^{-1}$ ) confirms a strong polarization of the CO molecule by the adsorbing sites ( $\Delta\nu(\text{CO}) = +38 \text{ cm}^{-1}$ ). The component at 2177  $\text{cm}^{-1}$  has been ascribed to CO adsorbed on strong bridging Brønsted acidic sites. By increasing the CO coverages, a gradual shift of the maximum to 2174  $\text{cm}^{-1}$  can be seen (spectrum 8). This shift is the result of a gradual cage filling<sup>32</sup> with formation of multi-adducts. Higher CO pressures also lead to interactions between CO and silanol groups, giving the component at 2164  $\text{cm}^{-1}$  (evident from spectrum 8). Furthermore, in the upper part of Figure 4a (spectra 9–15), the formation of Si–OH $\cdots$ CO adducts is testified by the erosion of the complex band with maxima at 3740–3712  $\text{cm}^{-1}$  and the parallel growth of a doublet at 3645 and 3587  $\text{cm}^{-1}$ . The isosbestic point at 3690  $\text{cm}^{-1}$  confirms a direct relation between the two species. Finally, the band representing H-bonded silanols (i.e., the previously described silanol nests), originally giving the broad band at 3500  $\text{cm}^{-1}$ , undergoes a continuous downward shift, eventually ending up at 3430  $\text{cm}^{-1}$ . This phenomenon can be explained by polarization of the O–H bonds from formation of H-bonded adducts at the terminal OH groups of the chain.<sup>29</sup> The last collected spectrum (spectrum 15) shows that at high CO loadings all bands broaden and all maxima progressively shift to lower frequencies. Also in the CO stretching frequency region (Figure 4b), a gradual red shift of all components can be observed. In particular, the band associated with CO interacting with strong Brønsted sites becomes less defined and the maximum red shifts to 2165  $\text{cm}^{-1}$ , while the component arising from interaction with silanols increases in intensity and shifts to 2157  $\text{cm}^{-1}$ . All these phenomena can be rationalized on the basis of CO polyaddition and formation of multilayered CO adsorption. Finally, the formation of a condensed phase is evidenced by the growth of a very strong absorption at 2138  $\text{cm}^{-1}$ —diagnostic of liquidlike CO.

All present experimental data confirm that H-SSZ-13 is a strongly acidic zeolite with two distinct families of Brønsted sites denoted HF and LF. These two families behave slightly differently upon CO adsorption, although the characteristics of the  $\text{OH}\cdots\text{CO}$  adducts formed on both sites are impossible to differentiate. This brings us to one of the essential points of this contribution since the presence of two distinct Brønsted bands have already been substantiated and assigned by combining 5 K neutron powder diffraction (on D-SSZ-13) and room-temperature DRIFT spectroscopy (on H-SSZ-13).<sup>8</sup> In that work, which has served as a basis for numerous later theoretical studies,<sup>12–14,33,34</sup> Cheetham and co-workers reported a higher population of deuterons at the O(1) and O(2) sites. The deuteron on O(1) was found to lie only 19° off the plane of the Si–O–Al bridge, pointing toward the center of the supercage, while the O(2) deuteron was found to be tilted toward the center of the six-membered ring at an angle of 45° from its corresponding plane at a distance of 2.64 Å from the O(3) oxygen of the six-membered ring. This geometry was suggested to induce an

H-bonding stabilization justifying the presence of two distinct  $\nu(\text{OH})$  absorptions (maxima at 3603 and 3579  $\text{cm}^{-1}$ ) for which a different acidity was claimed. The present data illustrate that, toward CO, both the LF and HF sites have the same acidity and that the only difference is the LF component starts to interact at higher CO pressures. An interpretation in line with our data is that the LF band represents the only oxygen not exposed to the eight-membered-ring window, that is, O(3) (see the Introduction and Figure 1 for further details). Contrary to the protons of the HF family, the proton bonded to O(3) will only be exposed to the environment of one single cage. Notice that this site is not populated according to Cheetham et al.<sup>8</sup> Moreover, we believe it is necessary to consider proton distributions among all four possible sites, both on the basis of two main points. First, the occupancy factors of the deuteriums on O(1) and O(2) are 0.083(9) and 0.040(4), respectively. Thus, the two sites are equally populated when symmetry is taken into account. Second, care has to be taken when comparing 5 K diffraction data with the hereby presented 70 K IR experiment because site rearrangements are likely when the thermal  $kT$  energy increases by more than 1 order of magnitude. This point is supported by theoretical calculations by Jeanvoine et al.<sup>12</sup> showing that the proton prefers the O(1) and O(2) sites, but the energetic difference with respect to O(3) and O(4) is within 7  $\text{kJ mol}^{-1}$ , a barrier easily surmountable at 70 K. As far as point one is concerned, note also that the integrated area of the LF band is much lower than that of the HF component (which is also characterized by a lower extinction coefficient). This means that the occupancy of the protons responsible for the LF component has to be significantly lower than that of the protons responsible for the HF component. This means that the attribution of the HF and LF bands to the almost equipopulated protons on O(1) and O(2), respectively, is not consistent. Conversely, if we assume the presence of (at least at 70 K) a minor fraction of protons (below the detection limit of neutron powder diffraction) on site O(3) responsible for the less pronounced LF component and we assume that the HF component represents protons located on the remaining sites (indistinguishable by IR spectroscopy), the whole picture of experimental data available seems to be in harmony.

**3.2.2. Interactions between CO and H-SAPO-34.** The IR spectrum of pretreated H-SAPO-34 in the OH stretching region, represented by spectrum 1 of Figure 5a, is dominated by a doublet at 3627 (HF) and 3603  $\text{cm}^{-1}$  (LF). The HF component has the highest intensity, and as previously reported,<sup>8,35</sup> both bands can be ascribed to bridging hydroxyl groups with a strong Brønsted character. Similar to what has been observed for H-SSZ-13, the presence of a doublet has been explained in terms of two distinct structural sites. Also, in this case, a previous study has combined spectroscopic experiments with neutron powder diffraction. Accordingly, an occupancy of 4.0% for the deuteron attached to O(2) and 8.3% for the one attached to O(4) was found. Again, this site distribution does not consider that, based on IR data, the populations of the two sites are expected to be different, where the HF component is significantly more abundant.

The minor components at 3748, 3742, and 3676  $\text{cm}^{-1}$  are respectively assigned to Al-OH, Si-OH, and P-OH species located outside the microcrystals. At a low to intermediate CO coverage (spectra 2–10), the main doublet erodes with a parallel growth of a composite band with a maximum at 3357  $\text{cm}^{-1}$  ( $\Delta\nu(\text{OH}) = -270 \text{ cm}^{-1}$ ) and a shoulder at 3340  $\text{cm}^{-1}$ . Note that, as was also observed for H-SSZ-13, the HF component is consumed faster than the LF component, indicating a more

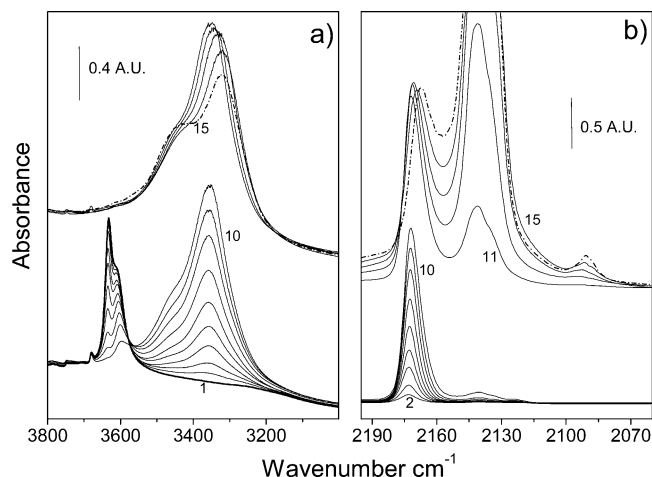


**Figure 5.** IR spectra of increasing dosages of CO at 70 K on H-SAPO-34 outgassed at 773 K. (a) OH stretching region (spectrum 1 represents the pretreated zeolite); (b) CO stretching region (background-subtracted spectra). The spectra have been divided into two subsets to distinguish 1:1 CO/Brønsted sites interactions (spectra 2–10) from effects associated with CO liquefied in the zeolitic cavities (spectra 11–15). Spectrum 15 (dash-dotted) reports the highest CO coverage.

difficult access to the LF sites. The intensity of the LF band furthermore decreases parallel to the growth of the shoulder at 3340  $\text{cm}^{-1}$ . This observation suggests a lower acidic character of the sites associated with the LF component in H-SAPO-34.<sup>35</sup> The formation of  $\text{OH}\cdots\text{CO}$  adducts can be followed also by considering the perturbation of the  $\nu(\text{CO})$  mode, as illustrated by the background-subtracted spectra 2–15 in Figure 5b. Starting from a low coverage (spectrum 2), a component is clearly visible at 2173  $\text{cm}^{-1}$ . The evident blue shift with respect to the free molecule ( $\Delta\nu(\text{CO}) = +35 \text{ cm}^{-1}$ ) confirms a polarization of the CO molecule by strong bridging Brønsted acidic sites (HF component). At higher coverages (spectrum 10), the main band becomes asymmetric, showing an evident tail on its low-frequency side. This behavior indicates growth of a second component associated with the formation of adducts between CO and less acidic hydroxyl species (LF), in agreement with the description of Figure 5a.

At high CO loadings (spectra 11–15), all bands broaden and show progressive shifts, suggesting multilayer addition effects. In particular, the band at 3440  $\text{cm}^{-1}$  has a blue shift to 3450  $\text{cm}^{-1}$ , while the component at 3357  $\text{cm}^{-1}$  has a red shift to 3321  $\text{cm}^{-1}$ . Notice the very broad shape of spectrum 15 (dash-dotted curve). In the CO stretching region there is no clear evidence of CO interacting with terminal OH groups and the main feature is a strong component at 2140  $\text{cm}^{-1}$  due to liquidlike CO.

On the basis of the perturbations of the Brønsted sites and the corresponding polarization of adsorbed CO, we can state that, compared to H-SSZ-13, H-SAPO-34 appears to interact slightly weaker with the probe molecule. Though not conclusive, the results suggest H-SSZ-13 to be the strongest Brønsted acid. However, such differences might be more evident from other probe molecules, and extended studies are in progress.

#### 4. Conclusions

In this work, adsorption of CO on H-SSZ-13 and H-SAPO-34 has been examined by transmission FTIR spectroscopy at 70 K. The Brønsted sites of H-SSZ-13 are composed of two families of OH groups: one family has an IR stretching frequency at 3616  $\text{cm}^{-1}$  (HF) and the other has an IR stretching frequency at 3584  $\text{cm}^{-1}$  (LF). Upon interaction with CO, it is

clear that the HF component erodes faster, confirming an easier access to the sites represented by this band. The acidity of the two families of sites appears to be the same, because they form OH $\cdots$ CO adducts with the same characteristics. In contrast to previous works, our data suggest that the LF band represents the only proton not directly exposed to the eight-membered-ring window. The LF proton is thus isolated from neighboring cages. The remaining three protons, all located on the eight-membered-ring windows giving access to the cage, are represented by the HF band. It is thus essential to consider proton distributions among all four sites, and not limit the interpretations exclusively to two sites.

On the basis of the perturbations of the Brønsted sites and the corresponding polarization of adsorbed CO, it appears that, compared to H–SSZ-13, H–SAPO-34 interacts slightly weaker with the probe molecule. It should be underlined that the differences are small and not conclusive. In H–SAPO-34, the LF band is associated with sites having lower acidity compared to species represented by the HF component.

**Acknowledgment.** M.B. is grateful for financial support from the Norwegian Research Council through Grant 158552/441. S.B. acknowledges MIUR for financial support through the NIS Centre of Excellence and INSTM through the PRIS-MA03 project. The authors are indebted to Prof. Adriano Zecchina and Prof. Giuseppe Spoto for fruitful discussions throughout the course of this work.

## References and Notes

- (1) Rabo, J. A.; Pellet, R. J.; Coughlin, P. K.; Shamson, E. S. *Zeolites as catalysts and detergent builders*; In Karge, H. G., Weitkamp, J., Eds.; Elsevier: Amsterdam, 1989.
- (2) Stöcker, M. *Microporous Mesoporous Mater.* **1999**, *29*, 3–48.
- (3) Chen, J.; Wright, P. A.; Natarajan, S.; Thomas, J. M. *Stud. Surf. Sci. Catal.* **1994**, *84*, 1731–1738.
- (4) Aufdembrink, B. A.; Dee, D. P.; McDaniel, P. L.; Mebrahtu, T.; Slager, T. L. *J. Phys. Chem. B* **2003**, *107*, 10025–10031.
- (5) Frache, A.; Gianotti, E.; Marchese, L. *Catal. Today* **2003**, *77*, 371–374.
- (6) Smith, L. J.; Cheetham, A. K.; Morris, R. E.; Marchese, L.; Thomas, J. M.; Wright, P. A.; Chen, J. *Science* **1996**, *271*, 799–801.
- (7) Gale, J. D.; Shah, R.; Payne, M. C.; Stich, I.; Terakura, K. *Catal. Today* **1999**, *50*, 525–532.
- (8) Smith, L. J.; Davidson, A.; Cheetham, A. K. *Catal. Lett.* **1997**, *49*, 143–146.
- (9) Shah, R.; Gale, J. D.; Payne, M. C. *J. Phys. Chem.* **1996**, *100*, 11688–11697.
- (10) Shah, R.; Gale, J. D.; Payne, M. C. *Chem. Commun.* **1997**, 131–132.
- (11) Jeanvoine, Y.; Ángyán, J. G.; Kresse, G.; Hafner, J. *J. Phys. Chem. B* **1998**, *102*, 7307–7310.
- (12) Jeanvoine, Y.; Ángyán, J. G.; Kresse, G.; Hafner, J. *J. Phys. Chem. B* **1998**, *102*, 5573–5580.
- (13) Sierka, M.; Sauer, J. *J. Chem. Phys.* **2000**, *112*, 6983–6996.
- (14) Civalleri, B.; Ferrari, A. M.; Llunell, M.; Orlando, R.; Mèrawa, M.; Ugliengo, P. *Chem. Mater.* **2003**, *15*, 3996–4004.
- (15) Lok, M. B.; Messina, C. A.; Patton, R. L.; Gajek, R. T.; Cannan, T. R.; Flanigen, E. M. U.S. Patent 4,440,871, 1984, examples 35 and 36.
- (16) Zones, S. I. U.S. Patent 4,544,538, 1985. Zones, S. I. Private communication.
- (17) Brunauer, S.; Emmett, P. H.; Teller, E. *J. Am. Chem. Soc.* **1938**, *60*, 309–319.
- (18) Langmuir, I. *J. Am. Chem. Soc.* **1916**, *38*, 2267; *J. Am. Chem. Soc.* **1918**, *40*, 1361–1402; *Phys. Rev.* **1916**, *8*, 149–176.
- (19) (a) de Boer, J. H.; van den Heuvel, A.; Linsen, B. G. *J. Catal.* **1964**, *3*, 268–273. (b) de Boer, J. H.; Linsen, B. G.; van der Plas, Th. J.; Zondervan, G. J. *J. Catal.* **1965**, *4*, 649–653. (c) de Boer, J. H.; Linsen, B. G.; Osinga, T. J. *J. Catal.* **1965**, *4*, 643–648. (d) de Boer, J. H. *J. Catal.* **1965**, *4*, 319–323. (e) Cranston, R.; Inkley, F. *Adv. Catal.* **1957**, *9*, 143–154. (f) Harkins, W. D.; Jura, G. *J. Chem. Phys.* **1943**, *11*, 431–432.
- (20) (a) Spoto, G.; Gribov, E.; Ricchiardi, G.; Damin, A.; Scarano, D.; Bordiga, S.; Lamberti, C.; Zecchina, A. *Prog. Surf. Sci.* **2004**, *76*, 71–146. (b) Gribov, E. N.; Bertarione, S.; Scarano, D.; Lamberti, C.; Spoto, G.; Zecchina, A. *J. Phys. Chem. B* **2004**, *108*, 16174–16186. (c) Spoto, G.; Gribov, E.; Bordiga, S.; Lamberti, C.; Ricchiardi, G.; Scarano, D.; Zecchina, A. *Chem. Commun.* **2004**, 2768–2769.
- (21) Villaescusa, L. A.; Bull, I.; Wheatley, P. S.; Lightfoot, P.; Morris, R. E. *J. Mater. Chem.* **2003**, *13*, 1978–1982.
- (22) Milanesio, M.; Artioli, G.; Gualtieri, A. F.; Palin, L.; Lamberti, C. *J. Am. Chem. Soc.* **2003**, *125*, 14549–14558.
- (23) Knöttinger, H.; Huber, S. *J. Chem. Soc., Faraday Trans.* **1998**, *94*, 2047–2059.
- (24) Zecchina, A.; Spoto, G.; Bordiga, S. In *Handbook of vibrational spectroscopy*; Wiley and Sons: New York, 2001; Vol. 4, pp 3042–3071.
- (25) Zecchina, A.; Otero Areán, C. *Chem. Soc. Rev.* **1996**, *25*, 187–195.
- (26) Bordiga, S.; Escalona Platero, E.; Otero Areán, C.; Lamberti, C.; Zecchina, A. *J. Catal.* **1992**, *137*, 179–185.
- (27) (a) Zecchina, A.; Bordiga, S.; Lamberti, C.; Spoto, G.; Carnelli, L.; Otero Areán, C. *J. Phys. Chem.* **1994**, *98*, 9577–9582. (b) Bordiga, S.; Lamberti, C.; Geobaldo, F.; Zecchina, A.; Turnes, P. G.; Otero, A. C. *Langmuir* **1995**, *11*, 527–533.
- (28) Zecchina, A.; Bordiga, S.; Spoto, G.; Scarano, D.; Petrini, G.; Leofanti, G.; Padovan, M.; Otero, A. C. *J. Chem. Soc., Faraday Trans.* **1992**, *88*, 2959–2969.
- (29) Zecchina, A.; Bordiga, S.; Spoto, G.; Marchese, L.; Petrini, G.; Leofanti, G.; Padovan, M. *J. Phys. Chem.* **1992**, *96*, 4991–4997.
- (30) Bordiga, S.; Ugliengo, P.; Damin, A.; Lamberti, C.; Spoto, G.; Spanò, G.; Buzzoni, R.; Dalloro, L.; Rivetti, L. *Top. Catal.* **2001**, *15* (1), 43–52.
- (31) Bordiga, S.; Roggero, I.; Ugliengo, P.; Zecchina, A.; Bolis, V.; Artioli, G.; Buzzoni, R.; Marra, G. L.; Rivetti, F.; Spanò, G.; Lamberti, C. *J. Chem. Soc., Dalton Trans.* **2000**, 3921–3929.
- (32) Zecchina, A.; Otero Areán, C.; Turnes Palomino, G.; Geobaldo, F.; Lamberti, C.; Spoto, G.; Bordiga, S. *Phys. Chem. Chem. Phys.* **1999**, *1*, 1649–1657.
- (33) (a) Mihaleva, V. V.; van Santen, R. A.; Jansen, A. P. *J. Chem. Phys.* **2003**, *119*, 13053–13060. (b) Mihaleva, V. V.; van Santen, R. A.; Jansen, A. P. *J. Chem. Phys.* **2004**, *120*, 9212–9221.
- (34) (a) Ugliengo, P.; Civalleri, B.; Zicovich-Wilson, C. M.; Dovesi, R. *Chem. Phys. Lett.* **2000**, *318*, 247–255. (b) Corà, F.; Catlow, C. R. A.; Civalleri, B.; Orlando, R. *J. Phys. Chem. B* **2003**, *107*, 11866–11870.
- (35) Smith, L.; Cheetham, A. K.; Marchese, L.; Thomas, J. M.; Wright, P. A.; Chen, J.; Gianotti, E. *Catal. Lett.* **1996**, *41*, 13–16.